Title

Hybrid ZTE/Dixon MR-based attenuation correction for quantitative uptake estimation of pelvic lesions in PET/MRI

Authors

Leynes, Andrew P
Yang, Jaewon
Shanbhag, Dattesh D
et al.

Peer reviewed

Hybrid ZTE/Dixon MR-based attenuation correction for quantitative uptake estimation of pelvic lesions in PET/MRI

Andrew P. Leynes and Jaewon Yang
Department of Radiology and Biomedical Imaging, University of California San Francisco, 1700 4th St, San Francisco, CA 94158, USA

Dattesh D. Shanbhag and Sandeep S. Kaushik
GE Global Research, Plot #122, Export Promotion Industrial Park, Phase 2, Hoodi Village, Whitefield Road, Bangalore 560066, India

Youngho Seo
Department of Radiology and Biomedical Imaging, University of California San Francisco, 1700 4th St, San Francisco, CA 94158, USA
UC Berkeley–UCSF Graduate Program in Bioengineering, University of California, Berkeley and University of California, 1700 4th St, San Francisco, CA 94158, USA

Thomas A. Hope
Department of Radiology and Biomedical Imaging, University of California San Francisco, 1700 4th St, San Francisco, CA 94158, USA

Florian Wiesinger*
GE Global Research, Freisinger Landstrasse 50, 85748 Garching bei München, Germany

Peder E. Z. Larson[a],*
Department of Radiology and Biomedical Imaging, University of California San Francisco, 1700 4th St, San Francisco, CA 94158, USA
UC Berkeley–UCSF Graduate Program in Bioengineering, University of California, Berkeley and University of California, 1700 4th St, San Francisco, CA 94158, USA

Purpose: This study introduces a new hybrid ZTE/Dixon MR-based attenuation correction (MRAC) method including bone density estimation for PET/MRI and quantifies the effects of bone attenuation on metastatic lesion uptake in the pelvis.

Methods: Six patients with pelvic lesions were scanned using fluorodeoxyglucose (18F-FDG) in an integrated time-of-flight (TOF) PET/MRI system. For PET attenuation correction, MR imaging consisted of two-point Dixon and zero echo-time (ZTE) pulse sequences. A continuous-value fat and water pseudoCT was generated from a two-point Dixon MRI. Bone was segmented from the ZTE images and converted to Hounsfield units (HU) using a continuous two-segment piecewise linear model based on ZTE MRI intensity. The HU values were converted to linear attenuation coefficients (LAC) using a bilinear model. The bone voxels of the Dixon-based pseudoCT were replaced by the ZTE-derived bone to produce the hybrid ZTE/Dixon pseudoCT. The three different AC maps (Dixon, hybrid ZTE/Dixon, CTAC) were used to reconstruct PET images using a TOF-ordered subset expectation maximization algorithm with a point-spread function model. Metastatic lesions were separated into two classes, bone lesions and soft tissue lesions, and analyzed. The MRAC methods were compared using a root-mean-squared error (RMSE), where the registered CTAC was taken as ground truth.

Results: The RMSE of the maximum standardized uptake values (SUV_{max}) is 11.02% and 7.79% for bone ($N = 6$) and soft tissue lesions ($N = 8$), respectively, using Dixon MRAC. The RMSE of SUV-max for these lesions is significantly reduced to 3.28% and 3.94% when using the new hybrid ZTE/Dixon MRAC. Additionally, the RMSE for PET SUVs across the entire pelvis and all patients are 8.76% and 4.18%, for the Dixon and hybrid ZTE/Dixon MRAC methods, respectively.

Conclusion: A hybrid ZTE/Dixon MRAC method was developed and applied to pelvic regions in an integrated TOF PET/MRI, demonstrating improved MRAC. This new method included bone density estimation, through which PET quantification is improved. © *2017 American Association of Physicists in Medicine* [https://doi.org/10.1002/mp.12122]

1. INTRODUCTION

Accurate PET standard uptake values (SUVs) estimation is important for many applications such as tumor staging and treatment response monitoring. This is especially important for quantitative imaging studies, comparisons across systems (e.g. PET/CT, PET/MR, or different vendors), and comparisons to other imaging parameters (e.g. diffusion-weighted MRI). Accurate uptake quantification depends on accurate attenuation correction, which is a major challenge

faced by PET/MR systems. In PET/CT, 511 keV photon attenuation coefficients can be readily estimated from CT Hounsfield units using a bilinear model,[1] whereas in PET/MRI, MRI measures nuclear spin properties and lacks photon attenuation information. Thus, it is difficult to infer attenuation information from the MR images and inaccurate attenuation correction induces errors in the PET uptake estimates.

Currently, commercially available MRAC methods for body PET imaging use a fat/water map derived from a "Dixon" MRI sequence, where only attenuation of soft tissue fat and water components are considered and bone is neglected.[2,3] This leads to errors of about 10% in and around bony regions.[4–6] Conventional MR imaging approaches do not detect any signal from bone due to its very short-T2* relaxation time ($T2 \approx 0.4$ ms[7–9]). Bone density estimation, however, is important particularly in pelvis PET/MRI due to the significant amount of bone, which has the largest photon attenuation among all tissue types. Neglecting bone in the attenuation coefficient (AC) map leads to a large underestimation of PET uptake in and around bone.

Atlas-based methods are commonly used for MRAC in the brain and include bone. AC maps are generated from registering an atlas generated from transmission[10,11] or CT scans.[12–15] The challenge of atlas-based methods is that they do not completely account for patient-specific variations in bone structure and density.

To capture patient-specific bone information for MRAC, methods based on ultrashort echo-time (UTE)[16–20] and zero echo-time (ZTE) pulse sequences have been proposed. Transverse relaxation rate (R2*) maps have been measured using UTE to estimate discrete[17] or continuous-valued[18,19] attenuation coefficients for bone. The R2* maps from these methods, designed to detect the short-T2* of bone, are also sensitive to short-T2* values resulting from off-resonance particularly in regions of large magnetic susceptibility differences such as the sinuses and other short-T2* tissues such as tendons, all of which may be misclassified as bone. ZTE MRI has also demonstrated excellent bone depiction with proton-density-weighting.[21–24] The water- and fat-suppressed projection imaging (WASPI) method, a ZTE sequence that includes fat and soft tissue suppression, has been used to generate continuous-value bone attenuation coefficients.[25] The limitations of the WASPI method are that the suppression pulses are sensitive to off-resonance and will reduce the bone SNR, and this approach may misclassify other short-T2* tissues as bone. Misclassification of other short-T2* soft tissues or short-T2* from off-resonance as bone in current UTE and ZTE methods will lead to errors in PET uptake quantification due to the substantial bone photon attenuation coefficient assigned to the misclassified tissues.

This paper introduces a new hybrid MRAC method ("Hybrid ZTE/Dixon MRAC") through the combination of ZTE MRI (bone segmentation and density estimation) and Dixon MRI (water, fat, and air). The bone density estimation is based on recent work showing that, with proton-density-weighted ZTE MRI, the bone density in the head is found to be inversely proportional to the ZTE signal intensity, allowing for continuous-valued attenuation coefficient estimation.[22] In this paper, we demonstrate this relationship also applies in the pelvis, and implemented pelvis-specific continuous-valued bone attenuation coefficients estimation. We quantitatively analyzed the performance of this new purely MR-derived AC method using 18F-FDG-PET uptake values in metastatic lesions in the pelvis.

2. METHODOLOGY

2.A. MR attenuation coefficient map generation

Our hybrid ZTE/Dixon MRAC method uses ZTE and Dixon MRI pulse sequences to generate a continuous-valued MRAC map that can account for water, fat, bone, and air attenuation coefficients. Figure 1 depicts the flowchart for the proposed method, which includes bone segmentation, continuous-value bone mapping, the combination of Dixon-based pseudoCT and ZTE-based pseudoCT that we call "hybridization", PET image reconstruction, and data analysis. Each of these steps are described in greater detail below. Image processing was done using MATLAB (The MathWorks, Inc., Natick, Massachusetts, United States).

2.A.1. ZTE MR image preprocessing

The ZTE MR images were bias corrected using N4 bias correction[26] to eliminate intensity bias due to differing coil sensitivities. The ZTE images are normalized to soft tissue values using a histogram-based method[22] to eliminate signal intensity variability due to hardware- and software-scaling factors. The ZTE-normalized signal is a proton-density signal that has been scaled to have soft tissue values centered around 1.

2.A.2. Bone segmentation

Proton-density-weighted ZTE MR images display soft tissue, cortical bone, and air with high, moderate, and low signal intensity, respectively. Cortical bone in the shaft of the femur is distinct while cortical bone around the femoral head or in the lumbar is more difficult to distinguish from surrounding tissues. To enhance bone, high-pass filtering, logarithmic intensity rescaling,[21,23] and top hat morphological filtering[27] was applied.

Cortical bone segmentation was done using global thresholding to produce an initial bone mask. Morphological area opening[27] was applied to reduce noise, and the segmentation map was corrected manually based on image features and anatomical knowledge of bone locations. Spongious bone inside cortical bone was added by applying morphological closing[27] to eliminate cortical bone discontinuities followed by a 3-D filling operation. The bone segmentation process and intermediate images are shown in Fig. 2.
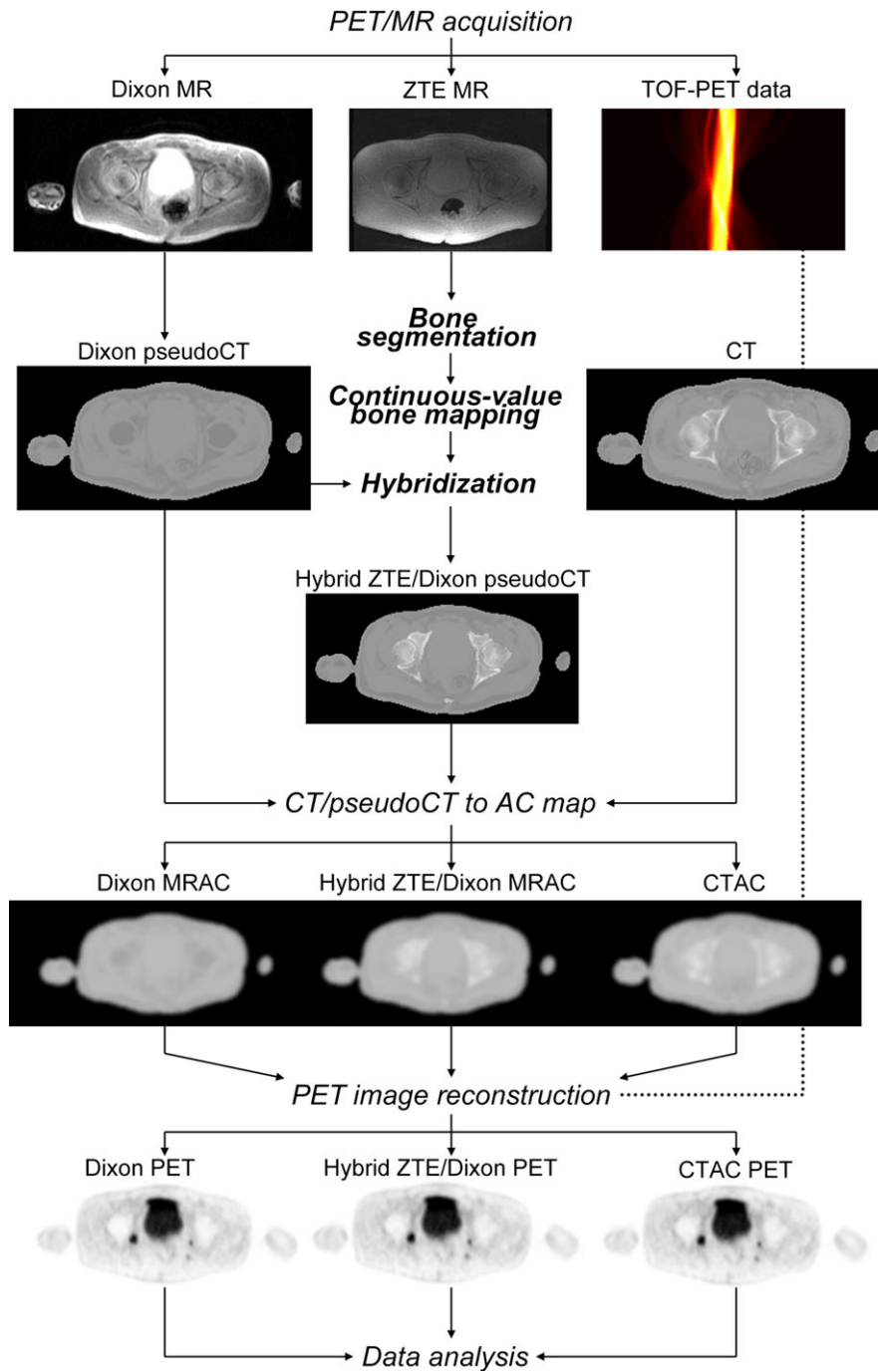
FIG. 1. Flowchart summarizing the methodology of the paper. Registered CT images are used as ground truth. The CT and pseudoCT images are converted to AC maps with a bilinear model. [Colour figure can be viewed at wileyonlinelibrary.com]

2.A.3. Continuous-value bone mapping

A continuous two-segment piecewise linear model was used to convert the ZTE-normalized signal (ZTE_{norm}) to HU values in segmented bone regions:

$$ZTEboneHU =$$
$$\begin{cases} slope1 * ZTE_{norm} + intercept1, ZTE_{norm} \leq threshold \\ slope2 * ZTE_{norm} + intercept2, ZTE_{norm} > threshold \end{cases} \quad (1)$$

Figure 3 shows the data used for generating this model, which was done using seven (7) co-registered CT and ZTE MRI patient datasets in the pelvis from our study. The images are co-registered using the same method discussed later in the paper. Multiple CT protocols were used for calibration with some variable parameter settings, but importantly the X-ray energy was constant across protocols (120 kVp, 99–375 mA, rotation time = 0.5 s, pitch = 0.6–0.98, 11.5–9.1 mm/rotation, axial FOV = 500–700 mm, slice thickness =
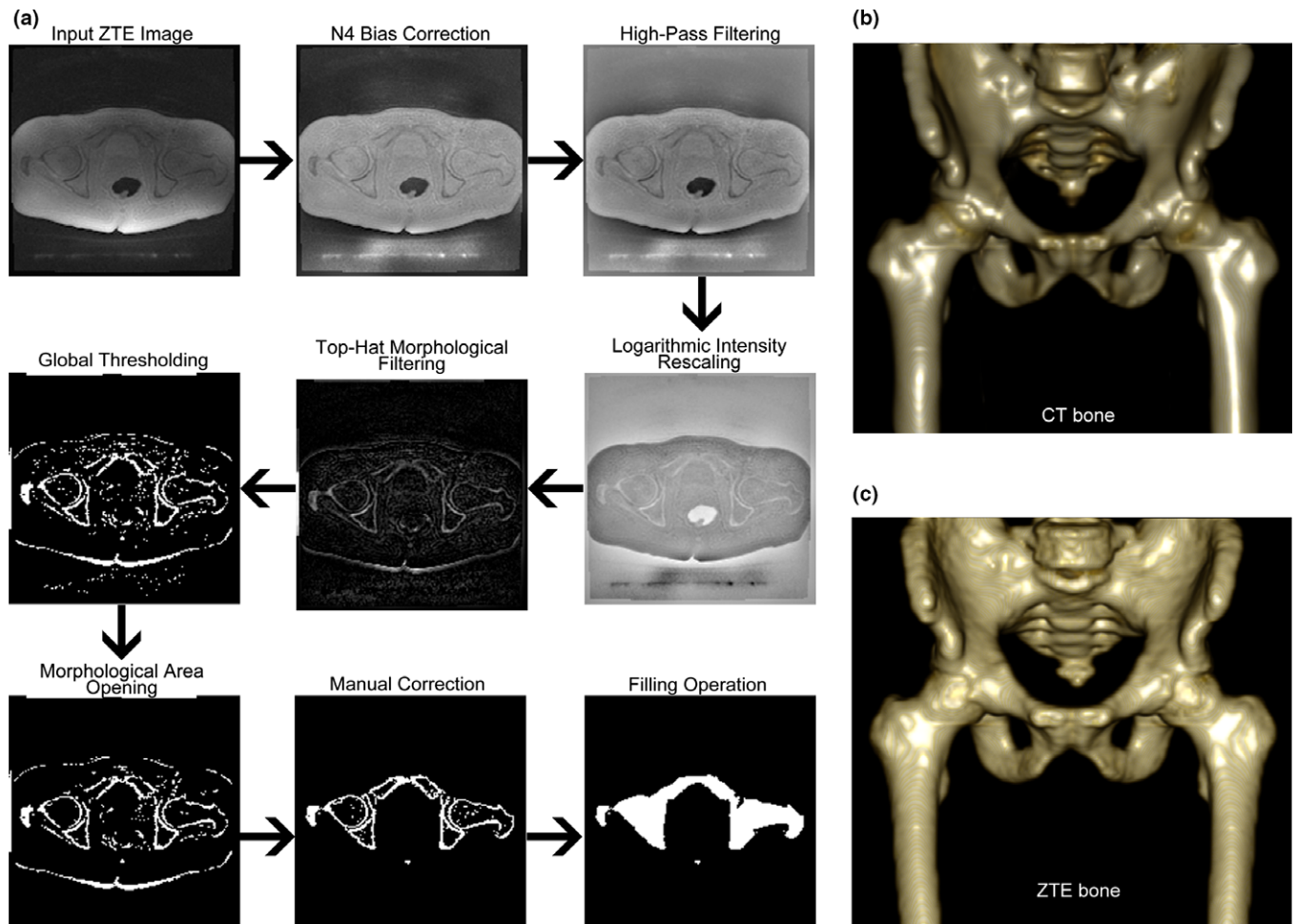
FIG. 2. Example images of each step of the bone segmentation process are shown in (a). 3-D rendering of the ZTE-segmented bone (c) shows strong visual similarity to CT-segmented bone (b). [Colour figure can be viewed at wileyonlinelibrary.com]

3–5 mm, matrix size = 512 × 512). Voxels used in the data were extracted by jointly segmenting bone from the ZTE images as described in Figure 2; and from the CT images using global thresholding (>−200HU). The calibration CT images were converted to the assumed energy of the Dixon pseudoCT, but yielding the same attenuation coefficients. Iteratively reweighted least squares was used to fit a two-segment piecewise linear model to the calibration data using the Shape Language Modeling toolkit.[28] This model was used in bone regions that were segmented using the process described earlier.

2.A.4. Hybridization

The hybrid ZTE/Dixon pseudoCT was generated by combining the Dixon continuous-valued fat and water pseudoCT[3] and the ZTE-derived continuous-valued bone HU. Bone voxels that were identified by the segmentation mask (*boneMask* $(\vec{x})$ = 1) were assigned the ZTE-derived continuous-value bone HU, $ZTEboneHU(\vec{x})$, otherwise the Dixon-derived HU, $DixonHU(\vec{x})$, value was used:

$$HybridHU(\vec{x}) = \begin{cases} ZTEboneHU(\vec{x}); boneMask(\vec{x}) = 1 \\ DixonHU(\vec{x}); otherwise \end{cases}$$

The CT and pseudoCT images were converted to linear attenuation coefficients (LAC) using a bilinear model.[1]

2.B. Patient studies

The study has been approved by the institutional review board (IRB) and all patients signed an informed consent form. Six patients with pelvic lesions (Table I) and one patient without pelvic lesions were scanned using an integrated 3 Tesla time-of-flight (TOF) PET/MRI system[29] (SIGNA PET/MR, GE Healthcare, Waukesha, WI, USA).

2.B.1. PET/MR imaging

The PET images were acquired with 18F-Fluorodeoxyglucose (18F-FDG). PET has 600 mm transaxial field-of-view (FOV) and 25 cm axial FOV, with TOF timing resolution of approximately 400 psec. The imaging protocol included a six
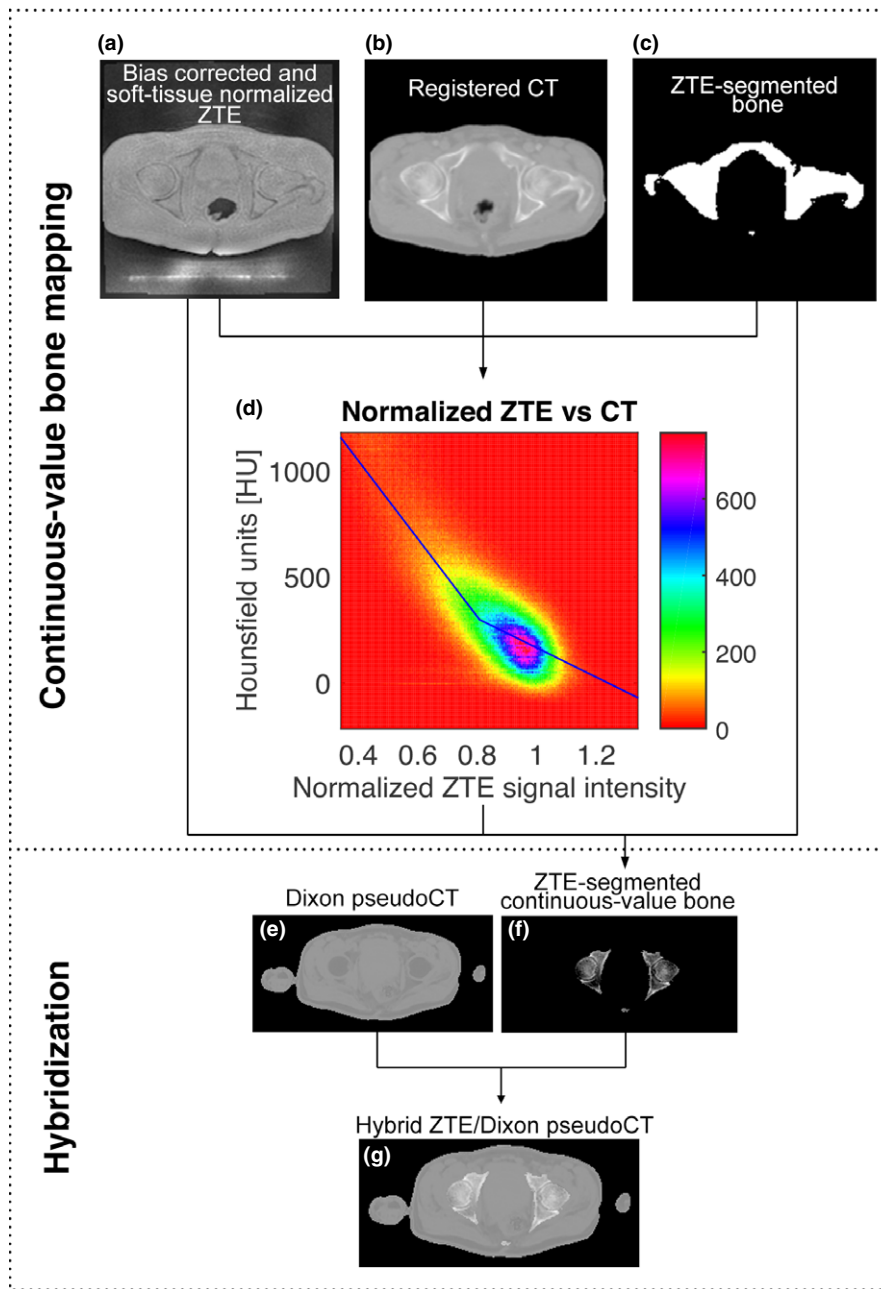
FIG. 3. Coregistered ZTE (a) and CT (b) images were used to produce a linear model to convert the normalized ZTE signal intensity to Hounsfield units. Only bone voxels as defined by the bone mask (c) are used in the modeling. Iteratively reweighted least squares fitting was used to produce the continuous two-segment piecewise linear model (d). The hybridization step combines the Dixon pseudoCT (e) and ZTE-segmented continuous-valued bone (f) using the linear model in (d) to produce the hybrid ZTE/Dixon pseudoCT (g). [Colour figure can be viewed at wileyonlinelibrary.com]

TABLE I. Patient demographics and disease diagnoses.

Patient #	Age	Sex	Disease Diagnosis
1	56	Male	Lung cancer
2	59	Female	Rectal cancer
3	61	Male	Rectal cancer
4	56	Male	Rectal cancer
5	59	Male	Rectal cancer
6	58	Female	Rectal cancer

bed position whole-body PET/MRI as well as a dedicated pelvic PET/MRI acquisition. The PET data were acquired for 15 min during the dedicated pelvis acquisition, during which time clinical MRI sequences as well as the Dixon and ZTE MR data were acquired.

A two-point Dixon pulse sequence was acquired for classification of fat and water soft tissues (FOV = 500 × 500 × 312 mm, resolution = 1.95 × 1.95 mm, slice thickness = 5.2 mm, slice spacing = 2.6 mm, BW = ± 166.67 kHz, TE = [1.15 ms, 2.3 ms], TR = 4.05 ms, partial Fourier along slice phase encode direction, scan time =

18 s, body transmit/receive coil). Proton density-weighted ZTE MRI was acquired for bone density estimation (cubical FOV = $(340 \text{ mm})^3$, isotropic resolution = $(2 \text{ mm})^3$, 28,900 radial views, BW = ± 62.5 kHz, 1.36 ms readout duration, FA = 0.6°, 4 μs hard RF pulse, scan time = 123 s) using automatically selected receive coils within the pelvis FOV from a whole-body receive array. Conventional gridding with sum-of-squares coil combination was used for the ZTE images. PET images were reconstructed with a TOF-ordered subset expectation maximization (OSEM) algorithm including a point-spread function model[30] (FOV = 600 mm, 2 iterations, 28 subsets, matrix size = 192 × 192, 89 slices of 2.78 mm thickness).

2.B.2. CT imaging

Helical CT images of the patients were acquired separately on different machines (Discovery STE PET/CT GE Healthcare, Biograph 16 PET/CT Siemens Healthcare, Philips Gemini TF PET/CT, Revolution CT GE Healthcare, SOMATOM Definition AS Siemens Healthcare, SOMATOM Force Siemens Healthcare) and are coregistered to the MR images. Multiple CT protocols were used with variable parameter settings (90–120 kVp, 90–706 mA, rotation time = 0.5 s, pitch = 0.6–1.2, 11.5–69.1 mm/rotation, axial FOV = 340–700 mm, slice thickness = 1–5 mm, matrix size = 512 × 512). Anatomical matching was performed between the CT and Dixon MRI using the methodology as described in ref. 31. Following anatomical matching, rigid registration was performed using affine transform and mutual information metric and was applied to the CT data. The anatomical matching and rigid registration pipeline was implemented using ITK (v. 4.7.2).[26] The rigidly aligned CT data were next registered to Dixon MRI using a diffeomorphic dense nonrigid registration (NRR). The NRR was done using the ANTS registration package (v. 2.0.3).[32]

Because the CT images were obtained at a different time, there were some differences in the distribution of intrabody air. Therefore, air in CT images was filled in with the soft tissue HU values from the Dixon-derived pseudoCT to eliminate any difference due to the air distribution. Air on the CT images was segmented using global thresholding (<−200 HU). The HU value in each voxel defined by the air mask was replaced by the HU value from the Dixon pseudoCT, which corresponds to soft tissue HU values inside the body and air HU values outside the body. Additionally, the CT scan was acquired with arms up while the PET/MR scan was acquired with arms down. To eliminate arms as a variable, the arms were manually segmented on the Dixon pseudoCT and copied over to the CT images: the corresponding arm's voxels in the CT images were assigned the HU values of the Dixon pseudoCT.

2.B.3. ZTE and dixon MR coregistration

Even though ZTE and Dixon MRI data were acquired for same pelvis station, there was subject motion in between

acquisitions resulting in some differences in femur and hip positioning in one patient. For this patient, the ZTE data were aligned to Dixon MRI using affine transform followed by NRR with ANTS.

2.C. Data analysis

2.C.1. Image analysis

Attenuation coefficient maps and resulting PET reconstructions were compared across the entire pelvic PET FOV, with CTAC taken as ground truth. Images of the percentage difference from CTAC were computed to account for local and patient differences in tissue density, radiotracer activity, and uptake. The average (μ) and standard deviation (σ) of the percent error were computed across the PET FOV over voxels that met a minimum signal-to-noise (SNR) criteria. The root-mean-squared error (RMSE) was also computed ($RMSE = \sqrt{\mu^2 + \sigma^2}$, (eq. 2)) as in Ouyang et al.[4] to summarize the errors.

2.C.2. Lesion-based analysis

Metastatic lesions were analyzed to specifically assess the impact of the MRAC methods on clinically relevant features. Lesions were identified on the PET images by a board-certified radiologist. The lesions were classified into two categories: bone lesions, which are within 10 mm or surrounded by bone, and soft tissue lesions, which are at least 10 mm away from bony structures in all directions.

Maximum standardized uptake values ($SUV_{\max}$) were measured for each lesion for analysis. The average (μ), standard deviation (σ), and RMSE of the $SUV_{\max}$ percent error between the MRAC methods and CTAC were computed to compare the methods. A Wilcoxon signed-rank test was used to compare the $SUV_{\max}$ biases to CTAC between MRAC methods.

3. RESULTS

The linear model used to map normalized ZTE MRI signal intensity to HU is shown in Fig. 3. In this model, voxels containing only bone will have the lowest ZTE signal and are assigned the highest HU values, whereas voxels with larger soft tissue fractions will have higher ZTE signal and lower HU values. Fits to the training datasets resulted in slopes of −1836 and −691 and intercepts of 1782 and 857 HU and a threshold of 0.8 for the model shown in Eq. 1. The model is weighted significantly by spongious bone below 400 HU suggesting that spongious bone attenuation is more significant than cortical bone due to its abundance.

Representative attenuation coefficient maps are shown in Fig. 4. The Dixon MRAC is able to closely approximate soft tissue HU values, however, it is missing the bone information. With the addition of ZTE bone, the hybrid ZTE/Dixon
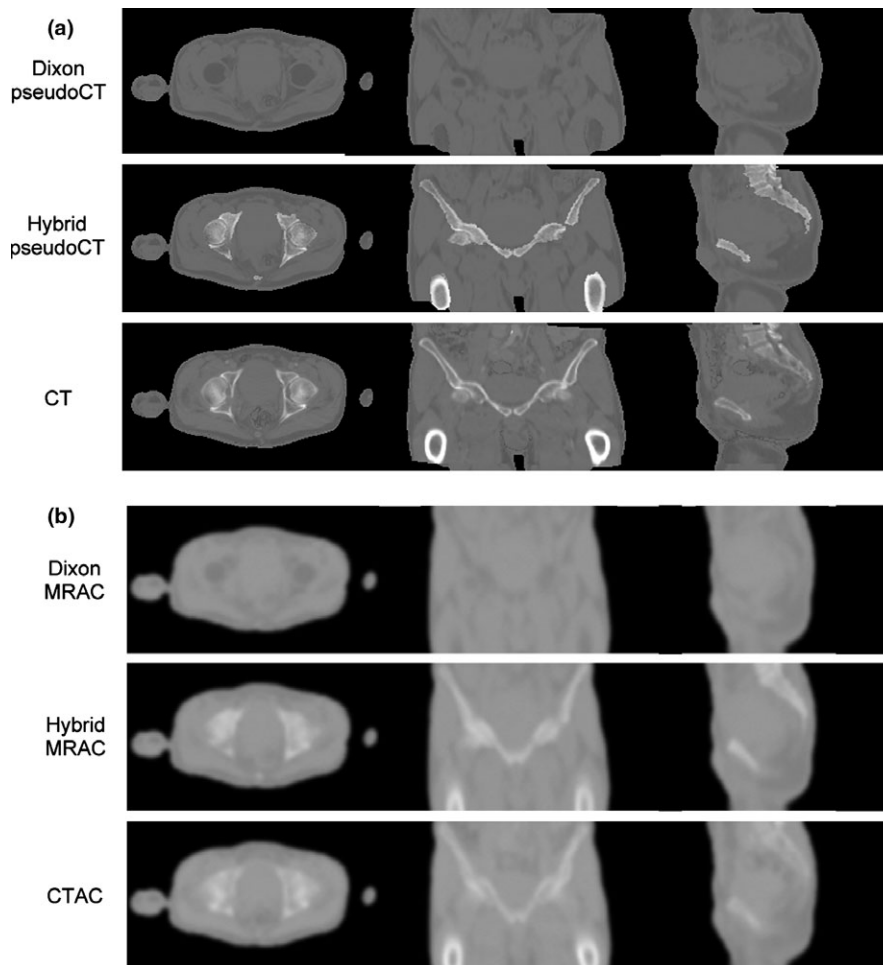
FIG. 4. Dixon pseudoCT (a, top row) and MRAC (b, top row) and hybrid ZTE/Dixon pseudoCT (a, middle row) and MRAC (b, middle row), vs CT (a, bottom row) and CTAC (c, bottom row) for patient #1. The ZTE-derived bone from Fig. 2 is added to the Dixon pseudoCT using the model proposed in Fig. 3. The bowel air and arms from the Dixon pseudoCT are copied to CT images to account for differences in air distribution and arm positioning.

MRAC appears similar to CTAC, capturing both the variations in bone density and soft tissue attenuation.

3.A. Image analysis

Difference images of the generated MRAC maps of the Dixon and Hybrid methods with the CTAC map are shown in Fig. 5. Dixon attenuation coefficients are constrained to values around 0.087 and 0.1 cm^{-1} due to the assignment of AC values based on the fractional fat and water maps. The addition of bone in the hybrid ZTE/Dixon MRAC extends the coverage of AC values above 0.1 cm^{-1} and gives a more linear relationship with CTAC. The RMSE for the difference between the MRAC methods and CTAC across the entire volume averaged across all patients within CTAC-segmented regions (>0.08 cm^{-1}) are 7.20% (Dixon, $\mu = -2.99\%$, $\sigma = 6.55\%$) and 4.64% (Hybrid, $\mu = -1.22\%$, $\sigma = 4.48\%$). The mean differences (μ) show that the Dixon MRAC has an underestimation bias, which is reduced by over a factor of 2 in the hybrid ZTE/Dixon MRAC. The standard deviations of the differences (σ) show that the hybrid ZTE/Dixon MRAC more consistently matches ground truth.

Sample CTAC 18F-FDG-PET and difference images when using the different MRAC methods are shown in Fig. 6. (Additional PET images from all AC methods are shown in Supplementary Figure S1.) The whole-volume RMSE between the PET reconstructed with the different MRAC methods and CTAC across all patients within CTAC PET-segmented regions (>0.5 SUV) are 8.76% (Dixon, $\mu = -6.14\%$, $\sigma = 6.25\%$) and 4.18% (Hybrid, $\mu = -2.57\%$, $\sigma = 3.31\%$). The underestimation bias observed in the Dixon MRAC results in an underestimation bias in the PET results as well; in comparison the mean is reduced by over a factor of 2 when using the hybrid ZTE/Dixon MRAC. As with the MRAC maps, the hybrid ZTE/Dixon PET also more consistently matches the ground truth.

3.B. Lesion analysis

Figure 7 shows results for metastatic lesions (six bone lesions and eight soft tissue lesions) in the pelvis. For bone lesions, the RMSE of the SUV_{max} between the MRAC methods and CTAC is 11.02% for Dixon MRAC ($\mu = -10.80\%$, $\sigma = 2.17\%$) and 3.28% for hybrid ZTE/
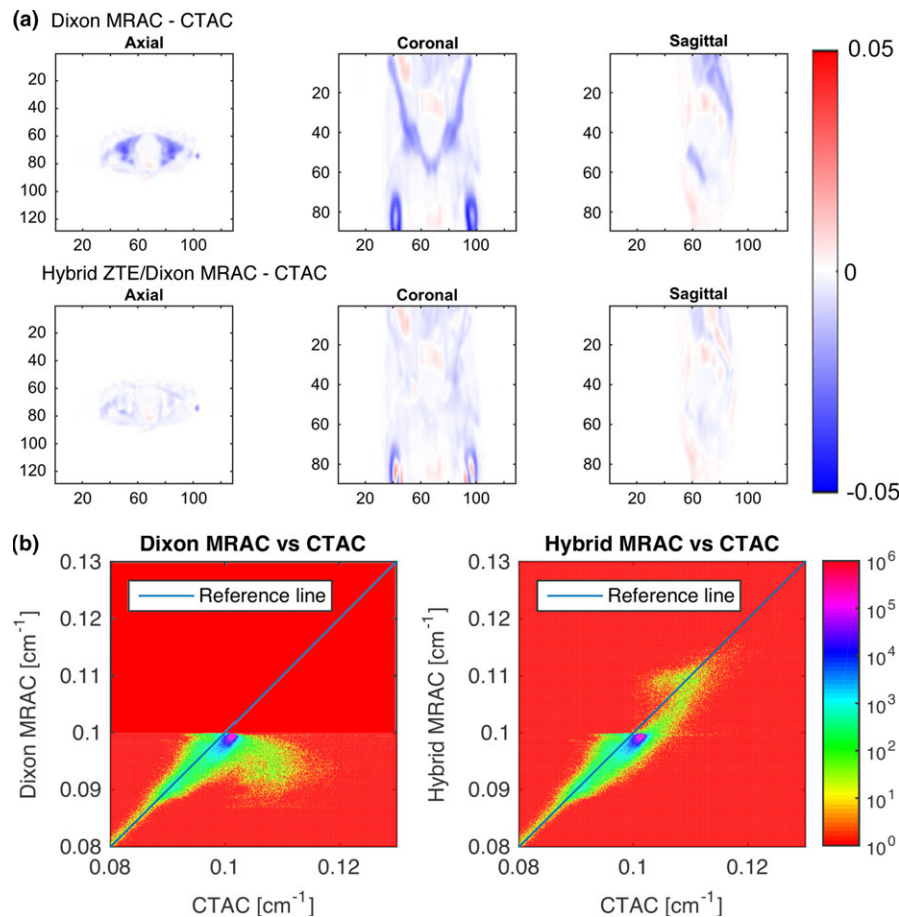
FIG. 5. Difference images between MR-based attenuation coefficient maps using Dixon MRAC (a, top row) and hybrid MRAC (a, middle row) and (b) joint histograms comparing to CTAC for patient #1. The underestimation of bone is seen in the difference images and the joint histogram for Dixon MRAC. This underestimation is largely eliminated by the addition of bone information in hybrid ZTE/Dixon MRAC. [Colour figure can be viewed at wileyonlinelibrary.com]

Dixon MRAC ($\mu = -3.17\%$, $\sigma = 0.85\%$). There is substantial underestimation bias with the Dixon MRAC that was significantly reduced *(P = 0.0312)* by the hybrid ZTE/Dixon MRAC method. The bone lesion errors with Dixon MRAC are much larger than whole-volume errors because they are most affected by the exclusion of accurate bone attenuation coefficients.

For soft tissue lesions, the RMSE is 7.79% for Dixon MRAC ($\mu = -7.67\%$, $\sigma = 1.36\%$) and 3.94% for hybrid ZTE/Dixon MRAC ($\mu = -3.54\%$, $\sigma = 1.71\%$). These lesions also showed a substantial underestimation bias with the Dixon MRAC that was significantly reduced *(P = 0.0078)* by the hybrid ZTE/Dixon MRAC method. Soft tissue lesion RMSE is reduced by a factor of 2, similar to the result with the whole-volume RMSE.

4. DISCUSSION

This paper presents a novel hybrid ZTE/Dixon attenuation correction method for PET/MRI and analyzes its performance in pelvic lesions. To our knowledge, this is the first method to incorporate bone attenuation for quantification of uptake in pelvic lesions using purely MR-derived data. The hybrid ZTE/Dixon MRAC demonstrated improved

quantitative uptake for pelvic lesions ($RMSE_{bone}$ = 3.28%, $RMSE_{soft\ tissue}$ = 3.94%) compared to the typically used fat/water Dixon MRAC ($RMSE_{bone}$ = 11.02%, $RMSE_{soft\ tissue}$ = 7.79%). When neglecting bone attenuation, the underestimation of uptake for bone lesions was greater than 10%. The underestimation in soft tissue lesions was not as marked (7.79%) due to their separation from bony structures but was still notable.

Prior research investigating the effect of bone attenuation in uptake quantification in bone and bone lesions reported underestimation values of $11.2 \pm 5.4\%$ (bone lesions),[5] $9.0 \pm 9.2\%$ (bone uptake),[4] and $15.3 \pm 2.3\%$ (bone lesions)[6] when bone attenuation is neglected. These studies simulated MRAC maps using PET/CT data. Concordant with their research, we report an underestimation of $10.80 \pm 2.17\%$ for bone lesions using purely MR-based attenuation correction. This growing body of work strongly suggests that accurate uptake estimation requires bone attenuation information in the pelvis.

Accurate uptake estimation is important for tumor staging and treatment response monitoring, and is especially so for quantitative imaging studies. This accuracy is important clinically when comparing across PET/CT and PET/MR systems or between vendors. For PET/MRI, spatial accuracy will be
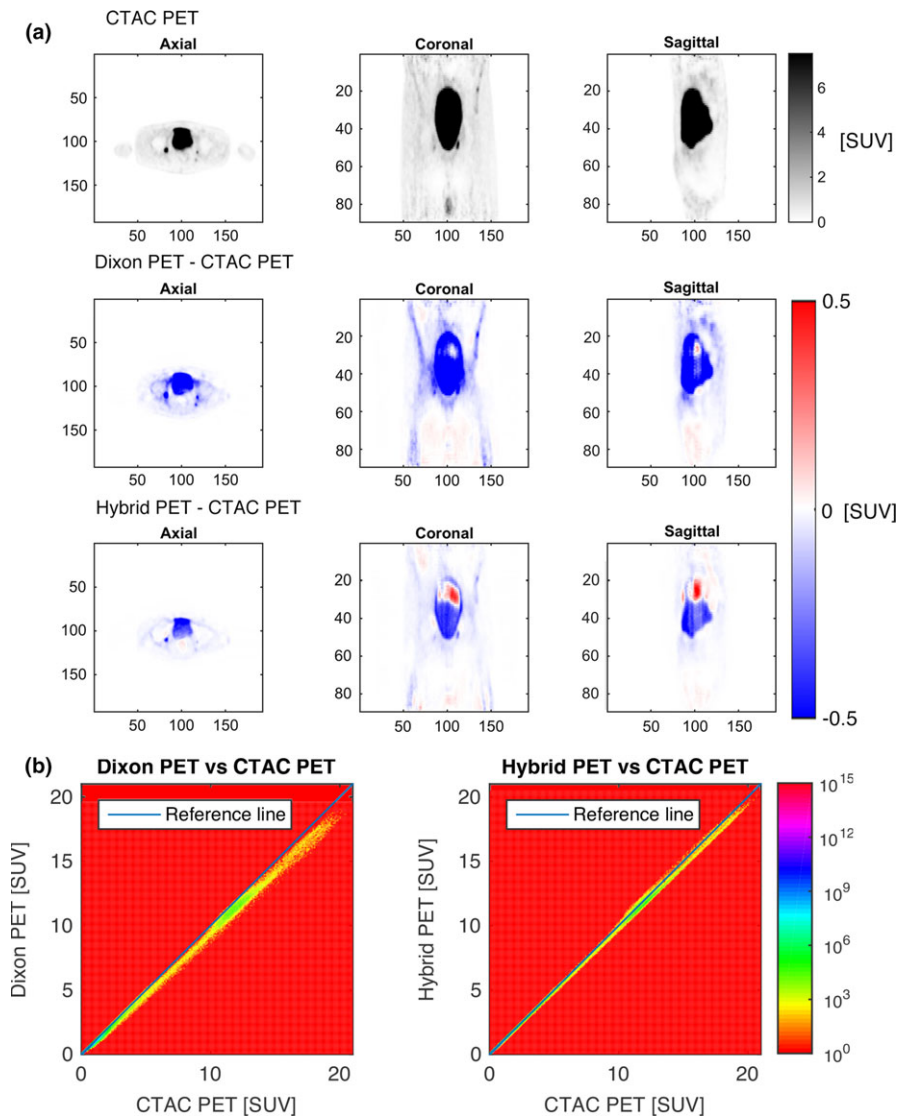
FIG. 6. Difference images comparing Dixon PET (a, middle row), hybrid PET (a, bottom row) with CTAC PET (a, top row), and joint histograms (b) with CTAC PET for patient #1. PET images from all AC methods are shown in Supplementary Figure S1. Uptake estimation in and around bone is underestimated in Dixon PET and is minimized by the addition of ZTE bone. The joint histograms indicate that Dixon PET is underestimating uptake over the whole image and is largely corrected by the addition of ZTE bone. Uptake in certain regions in the hybrid PET image is overestimated suggesting that bone is overestimated around those regions. [Colour figure can be viewed at wileyonlinelibrary.com]

very important to compare MRI parameters, for example, from diffusion-weighted imaging, with PET parameters. Pelvis PET/MR oncology studies, such as prostate cancer, cervical cancer, or rectal cancer studies, are directly impacted by our findings. Studies in other anatomic regions where a large amount of bone is present, such as the spine or the knee, will also likely benefit from the presented hybrid ZTE/Dixon MRAC method.

Our results demonstrate a significant reduction in uptake estimation errors when adding MR-derived bone attenuation, however, some bias still remains. This difference could be due to errors in soft tissue attenuation coefficients estimation Shown in Figure S2 are the 2D histograms comparing Dixon MRAC and CTAC, and Hybrid MRAC and CTAC for all patients. The soft tissue attenuation coefficients that dominate the histogram are

underestimated by the Dixon-based MRAC, possibly coming from differences in calibration of this method. The Dixon MRAC was calibrated with whole-body images,[3] so there could be differences in distribution of soft tissue attenuation coefficients in the pelvis. There may also be physiological differences that were not accounted for, such as bladder volume, between the MR images and reference CT data since the scans were not acquired in succession.

One challenge and limitation in our study was registration of CT and PET/MR images – a challenge with any multiscanner study. As the CT and MR were not acquired consecutively as in a trimodality system,[33] there were some noticeable registration errors, with largest errors due to femur alignment. However, we expect this does not substantially affect our results and conclusions because the registration errors are
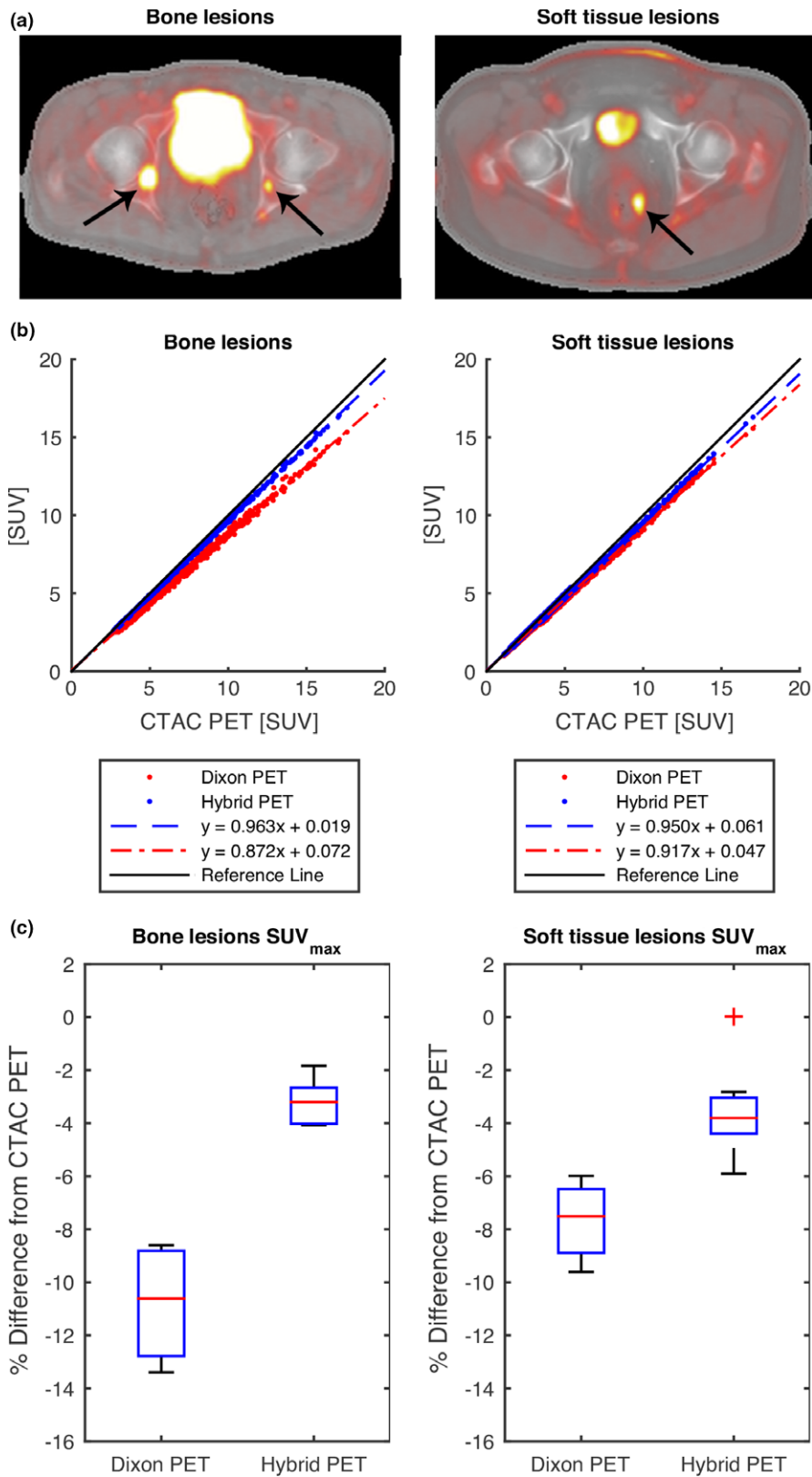
(a)

Bone lesions   **Soft tissue lesions**

(b)

(c)

FIG. 7. (a) Representative 18F-FDG-PET images overlaid on the registered CT images used for reconstruction, where arrows denote the metastatic lesions. (b) Scatter plots of pelvic lesion voxels in all patients between Dixon PET (left) and hybrid ZTE/Dixon PET (right) vs CTAC PET. The slope of the least-squares line in the scatter plots shows strong agreement of lesion uptake between the hybrid ZTE/Dixon MRAC and CTAC reconstructions. (c) Box plots of the SUVmax for bone (left) and soft tissue lesions (right). With the addition of bone in the hybrid ZTE/Dixon PET, the uptake of malignant lesions is better approximated as can be seen in (b) and (c). [Colour figure can be viewed at wileyonlinelibrary.com]

located sufficiently far away from the pelvic lesions such that there are no lesion lines-of-response that can be traced between them.

Another limitation of these results is that we analyzed a relatively small number of patients and lesion data. Within this constraint, calibration of the mapping of the ZTE signal to Hounsfield units included the six patients it was later applied to, which likely improved correlation between CT and the hybrid pseudoCT. However, this may not be a substantial improvement since a single mapping function was applied across all patients. This is an initial study to demonstrate that the concept, methodology, and feasibility of using proton-density-weighted ZTE to obtain continuous-valued LAC for bone in the pelvis. We will expand to a larger cohort for validation in future work.

In our comparison, air in CT images was filled in with the soft tissue HU values from the Dixon-derived pseudoCT to eliminate any difference due to the air distribution. Thus far, there have been no studies to explore the effect of bowel air in uptake estimation. The typically used Dixon MRAC replaces bowel air with soft tissue attenuation coefficients, which potentially compensates for the missing bone attenuation. However, the use of Dixon MRAC could possibly lead to more variance in uptake quantification, especially in lesions beside bowel air such as rectal lesions. Bowel air is also challenging because it may move during the PET scan. CT only provides a snapshot in time, while MRI requires longer scans but may also be able to provide time-averaged or -resolved air imaging. With our proposed method, an additional segmentation step can be performed to include bowel air in the hybrid ZTE/Dixon MRAC to potentially further improve uptake estimation. Due to our limitation of having CT and PET/MR scans acquired in different days, we could not sufficiently explore these ideas.

Finally, the presented bone segmentation process relies on a manual correction step and was based on anatomical knowledge of bone locations. As illustrated in Fig. 2, this is primarily done to remove segmentation errors at the edge of the body due to partial voluming and incorrectly segmented soft tissue due to noise. In order to be able to use the hybrid ZTE/Dixon MRAC in a clinical environment, this step would need to be automated. Since our manual correction was based on the operator's knowledge of where bones are located in the pelvis, we believe this step could readily be automated by incorporating anatomical prior information of bone structure through an imaging atlas[34–36] for a clinically suitable, fully automated bone segmentation.

5. CONCLUSION

We have presented a new hybrid ZTE/Dixon MRAC method that results in significantly improved uptake quantification for pelvic lesions. Studies in other anatomical regions where a large amount of bone is present, such as the spine or the knee, will also likely benefit from the presented hybrid ZTE/Dixon MRAC method.

ACKNOWLEDGMENTS

CONFLICT OF INTEREST

None.

*These authors contributed equally to this work
a)Author to whom correspondence should be addressed. Electronic mail: peder.larson@ucsf.edu; Telephone: +1 (415) 514-4876.

REFERENCES

1. Kinahan PE, Townsend DW, Beyer T, Sashin D. Attenuation correction for a combined 3D PET/CT scanner. *Med Phys*. 1998;25:2046–2053.
2. Martinez-Möller A, Souvatzoglou M, Delso G, et al. Tissue classification as a potential approach for attenuation correction in whole-body PET/MRI: Evaluation with PET/CT data. *J Nucl Med*. 2009;50:520–526.
3. Wollenweber SD, Ambwani S, Lonn AHR, et al. Comparison of 4-class and continuous fat/water methods for whole-body, MR-based PET attenuation correction. *IEEE Trans Nucl Sci*. 2013;60:3391–3398.
4. Ouyang J, Chun SY, Petibon Y, Bonab AA, Alpert N, El Fakhri G. Bias Atlases for segmentation-based PET attenuation correction using PET-CT and MR. *IEEE Trans Nucl Sci*. 2013;60:3373–3382.
5. Samarin A, Burger C, Wollenweber SD, et al. PET/MR imaging of bone lesions – implications for PET quantification from imperfect attenuation correction. *Eur J Nucl Med Mol Imaging*. 2012;39:1154–1160.
6. Mehranian A, Zaidi H. Impact of time-of-flight PET on quantification errors in MR imaging-based attenuation correction. *J Nucl Med*. 2015;56:635–641.
7. Horch RA, Nyman JS, Gochberg DF, Dortch RD, Does MD. Characterization of 1H NMR signal in human cortical bone for magnetic resonance imaging. *Magn Reson Med*. 2010;64:680–687.
8. Du J, Carl M, Bydder M, Takahashi A, Chung CB, Bydder GM. Qualitative and quantitative ultrashort echo time (UTE) imaging of cortical bone. *J Magn Reson*. 2010;207:304–311.
9. Krug R, Larson PEZ, Wang C, et al. Ultrashort echo time MRI of cortical bone at 7 tesla field strength: A feasibility study. *J Magn Reson Imaging*. 2011;34:691–695.
10. Malone IB, Ansorge RE, Williams GB, Nestor PJ, Carpenter TA, Fryer TD. Attenuation correction methods suitable for brain imaging with a PET/MRI scanner: A comparison of tissue Atlas and template attenuation map approaches. *J Nucl Med*. 2011;52:1142–1149.
11. Montandon M-L, Zaidi H. Atlas-guided non-uniform attenuation correction in cerebral 3D PET imaging. *NeuroImage*. 2005;25:278–286.
12. Schreibmann E, Nye JA, Schuster DM, Martin DR, Votaw J, Fox T. MR-based attenuation correction for hybrid PET-MR brain imaging systems using deformable image registration. *Med Phys*. 2010;37:2101–2109.
13. Sekine T, Buck A, Delso G, et al. Evaluation of atlas-based attenuation correction for integrated PET/MR in human brain: application of a head atlas and comparison to true CT-based attenuation correction. *J Nucl Med*. 2016;57:215–220.
14. Hofmann M, Bezrukov I, Mantlik F, et al. MRI-based attenuation correction for whole-body PET/MRI: Quantitative evaluation of segmentation- and Atlas-based methods. *J Nucl Med*. 2011;52:1392–1399.
15. Wollenweber SD, Ambwani S, Delso G, et al. Evaluation of an Atlas-based PET head attenuation correction using PET/CT amp; MR patient data. *IEEE Trans Nucl Sci*. 2013;60:3383–3390.
16. Keereman V, Fierens Y, Broux T, Deene YD, Lonneux M, Vandenberghe S. MRI-based attenuation correction for PET/MRI using ultrashort echo time sequences. *J Nucl Med*. 2010;51:812–818.

17. Berker Y, Franke J, Salomon A, et al. MRI-based attenuation correction for hybrid PET/MRI systems: A 4-class tissue segmentation technique using a combined ultrashort-echo-time/Dixon MRI sequence. *J Nucl Med*. 2012;53:796–804.

18. Navalpakkam BK, Braun H, Kuwert T, Quick HH. Magnetic resonance-based attenuation correction for PET/MR hybrid imaging using continuous valued attenuation maps. *Invest Radiol*. 2013;48:323–332.

19. Cabello J, Lukas M, Förster S, Pyka T, Nekolla SG, Ziegler SI. MR-based attenuation correction using ultrashort-echo-time pulse sequences in dementia patients. *J Nucl Med*. 2015;56:423–429.

20. Catana C, Van der Kouwe A, Benner T, et al. Toward implementing an MRI-Based PET attenuation-correction method for neurologic studies on the MR-PET brain prototype. *J Nucl Med*. 2010;51:1431–1438.

21. Wiesinger F, Sacolick LI, Menini A, et al. Zero TE MR bone imaging in the head. *Magn Reson Med*. 2015;75:107–114.

22. Wiesinger F, Kaushik SS, Shanbhag DD, et al. ZT-AC: Zero TE based PET/MR attenuation correction. *Proc Int Soc Magn Reson Med*. 2016;24:3559.

23. Delso G, Wiesinger F, Carl M, et al. ZTE-based clinical bone imaging for PET/MR. *J Nucl Med*. 2015;56:1806–1806.

24. Boss A, Weiger M, Wiesinger F. Future image acquisition trends for PET/MRI. *Semin Nucl Med*. 2015;45:201–211.

25. Huang C, Ouyang J, Reese TG, Wu Y, Fakhri GE, Ackerman JL. Continuous MR bone density measurement using water- and fat-suppressed projection imaging (WASPI) for PET attenuation correction in PET-MR. *Phys Med Biol*. 2015;60:N369.

26. Tustison NJ, Avants BB, Cook PA, et al. N4ITK: Improved N3 bias correction. *IEEE Trans Med Imaging*. 2010;29:1310–1320.

27. Gonzalez R, Woods R. *Digital Image Processing*. Upper Saddle River, NJ, USA: Prentice-Hall Inc; 2006.

28. D'Errico J. SLM – Shape Language Modeling – File Exchange – MATLAB Central. 2014.

29. Levin CS, Maramraju SH, Khalighi MM, Deller TW, Delso G, Jansen F. Design features and mutual compatibility studies of the time-of-flight PET capable GE SIGNA PET/MR system. *IEEE Trans Med Imaging*. 2016;35:1907–1914.

30. Alessio AM, Stearns CW, Tong S, et al. Application and evaluation of a measured spatially variant system model for PET image reconstruction. *IEEE Trans Med Imaging*. 2010;29:938–949.

31. Patel H, Gurumoorthy K, Thiruvenkadam S. Automatic determination of anatomical correspopndences for multimodal field of view correction. In: Jiang X, Hornegger J, Koch R, eds. *Pattern Recognition: 36th German Conference, GCPR 2014, Münster, Germany, September 2-5, 2014, Proceedings*. Cham: Springer International Publishing; 2014: 432–442.

32. Avants BB, Tustison NJ, Stauffer M, Song G, Wu B, Gee JC. The Insight ToolKit image registration framework. *Front Neuroinform*. 2014;8:44.

33. Veit-Haibach P, Kuhn FP, Wiesinger F, Delso G, von Schulthess G. PET–MR imaging using a tri-modality PET/CT–MR system with a dedicated shuttle in clinical routine. *Magn Reson Mater Phys Biol Med*. 2013;26:25–35.

34. Thompson S, Penney G, Buie D, Dasgupta P, Hawkes D. Use of a CT statistical deformation model for multi-modal pelvic bone segmentation. *Proc SPIE*. 2008;6914:69141O.

35. Liu L, Cao Y, Fessler JA, Jolly S, Balter JM. A female pelvic bone shape model for air/bone separation in support of synthetic CT generation for radiation therapy. *Phys Med Biol*. 2016;61:169.

36. Paulus DH, Quick HH, Geppert C, et al. Whole-body PET/MR imaging: Quantitative evaluation of a novel model-based MR attenuation correction method including bone. *J Nucl Med*. 2015;56: 1061–1066.

SUPPORTING INFORMATION

Additional Supporting Information may be found online in the supporting information tab for this article.

Figure S1. Reconstructed PET images using CTAC (top row), Dixon MRAC (middle row), and Hybrid ZTE/Dixon MRAC (bottom row) for patient #1.

Figure S2. 2D histograms comparing Dixon MRAC vs. CTAC and Hybrid MRAC vs. CTAC in linear scale (top row) and log scale (bottom row) containing data from all patients. Bone attenuation coefficients in the Hybrid MRAC are invisible when viewed in linear scale indicating that soft tissue attenuation coefficients dominate the histogram. This suggests that soft tissue attenuation coefficients cause the remaining error.